We are IntechOpen,
the world's leading publisher of
Open Access books
Built by scientists, for scientists

4,800
Open access books available

122,000
International authors and editors

135M
Downloads

154
Countries delivered to

Our authors are among the

TOP 1%
most cited scientists

12.2%
Contributors from top 500 universities

BOOK CITATION INDEX
CLARIVATE ANALYTICS
INDEXED

WEB OF SCIENCE™

Selection of our books indexed in the Book Citation Index
in Web of Science™ Core Collection (BKCI)

Interested in publishing with us?
Contact book.department@intechopen.com

Numbers displayed above are based on latest data collected.
For more information visit www.intechopen.com

Radial Shearing Interferometer

Naiting Gu and Qun Luo

Abstract

Radial shearing interferometer (RSI) is one of the most powerful tools in many domains, especially in optical testing. RSI has compact size and good vibration immunity, which is adaptive to various environments, due to its common-path configuration. Moreover, it is very convenient application because no plane referencing wavefront is needed. The disadvantages of the conventional RSIs are that the distorted wavefront is hard to extract quickly and accurately from one radial shearography due to the phase extract algorithm is complex. Fortunately, the new RSIs can receive benefits from the accuracy of the methods of phase-shifting interferometry, and phase-shifting shearography is more sensitive than simple digital shearography. There are two mainly trend to the RSIs based on phase-shifting technique, i.e. instantaneous phase-shifting and compact size. In this chapter, a development process of RSI will be introduced briefly firstly, and then the some new RSIs based phase-shifting techniques in our work will be described in following parts, including initial RSI by using four-step polarization phase-shifting, modal wavefront reconstruction method for RSI with lateral shear and a new kind of compact RSI based micro-optics technique.

Keywords: radial shearing interferometer, phase-shifting technique, instantaneous, vibration insensitive, modal wavefront reconstruction

1. Introduction

Radial shearing interferometer (RSI) was proposed firstly in 1961 [1]. After development of many years, the RSI has been used widely in optical testing [2–4], corneal topographic inspection [5–7], wavefront sensing [8–11] and laser beam characterization [12–14]. Radial shear can be introduced by some classical optical components [15, 16] and the other different ways [17–21] including optical gratings [17, 18], zone plate [19], speckle interference [20, 21] and the other applications. It is very convenient application because no plane referencing wavefront is needed [24], especially comparing to the point diffraction interferometer (PDI) [22, 23]. RSI has compact size and good vibration immunity, which is adaptive to various environments, due to its common-path configuration. Recently, RSI has been becoming one of the most important tools for diagnosing the wavefront of laser beams and the other applications. The disadvantages of the conventional RSIs are that the distorted wavefront is hard to extract from only one radial shearography due to the complexity of the phase extract algorithm. However, fortunately, many of these applications can receive benefits from the high accuracy of phase-shifting interference methods, and phase-shifting shearography is more sensitive than simple radial shearography [25]. Thus some authors [8, 26–28] have proposed several kinds of RSIs by using temporal or spatial phase-shifting

techniques. A cyclic RSI was developed in Ref. [26] for phase shifting interferometry with a polarization phase shifter. A RSI based on a Mach-Zehnder configuration by using liquid-crystal-device as the phase shifter was described in Ref. [27]. A Sagnac RSI with geometric phase-shifting technique was designed in Ref. [28]. However, all above these developed RSIs adopted the temporal phase shifting technique. In this case, the wavefront under test must be essentially stationary during the duration of acquiring several phase-stepping images, and they cannot be used to measure dynamic wavefront. In Ref. [8], a new RSI with spatial phase shifting techniques was developed for wavefront measurements and diagnosing dynamic measurements and the single-shot common-path phase-stepping configuration improved the performance of RSI especially for dynamic scenes. However, its complex configuration and extraction algorithm limits the testing accuracy, system stability, compactness and its application. Apparently, it is highly desirable to acquire compact one-shot vibration-insensitive RSIs. In Ref. [29], a new compact RSI with simultaneous phase-shifter based on a micro-retarder array (MRA) was proposed, which has some good features such as high speed, high accuracy and vibration immunity while decreasing the complexity. In Ref. [11], a new modal reconstruction algorithm was proposed to reconstruct accurately and quickly the wavefront under test in a RSI with or without lateral shear.

In this chapter, we will introduce the new RSIs with instantaneous phase-shifting and its corresponding modal wavefront reconstruction method. These works have been published earlier in [8, 11, 29], and they are re-arranged in this manuscript. This manuscript is organized as follows. In Section 2 a single-shot common-path phase-stepping RSI will be introduced. A new RSI with simultaneous phase-shifter based on a micro-retarder array will be described in Section 2.1. In Section 3 a modal wavefront reconstruction method based on Zernike polynomials in a RSI with or without lateral shear will be described. The conclusion of this chapter will be made in final section.

2. RSI based on simultaneous polarization phase-shifter

RSIs in many domains can receive advantages from the accuracy of phase-shifting interference methods, and many new RSIs were proposed by utilizing temporal or spatial phase-shifting techniques. Comparatively, the temporal phase shifting technique requires stationary scene during the duration of acquiring several phase-stepping images, but the spatial phase-shifting technique not. Thus the RSIs with spatial phase-shifting technique are preferred to apply in several applications due to its ability for dynamic scene. In this part we will introduce a new RSI based on simultaneous polarization phase-shifter.

2.1 System design and basic principle

Figure 1 shows the schematic diagram and its experimental setup of the RSI based on simultaneous polarization phase-shifter. It is composed of three main individual parts, i.e. wavefront simulator (WS), Hartmann-Shack wavefront sensor (HS WFS) and common-path phase-shifting RSI, which is the core part of this system. The proposed RSI includes a four-channel polarization phase stepper (FCPPS) and a cyclic RSI, which comprise a polarizing beam splitter (PBS1), two lenses (L5 and L6) and two flat mirrors (M1 and M2). The cyclic RSI can be treated as a Keplerian telescope system comprised L5 and L6. P2 is used to filter the state of polarization (SoP) of incident light at a fixed filtering angle. The passing beam will be guided into the RSI system and divided into two beams according to its
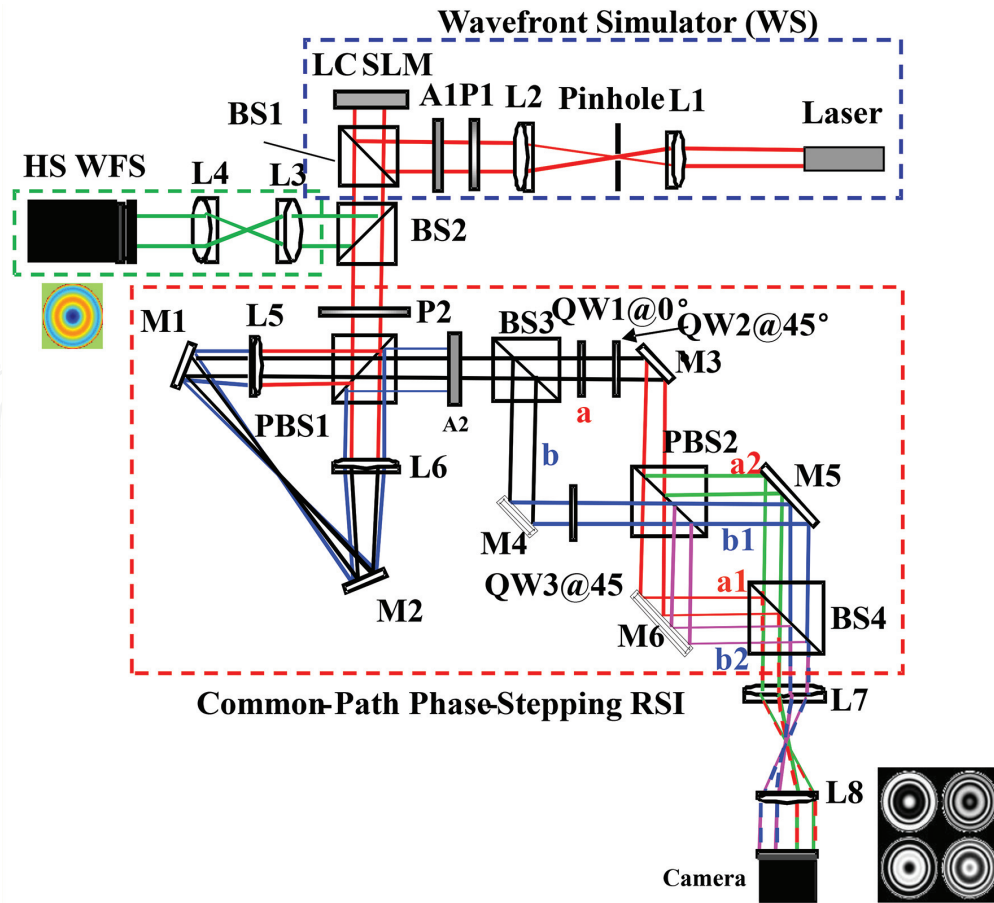
Figure 1.
Concept design and experimental setup of the RSI with spatial phase-shifting method. L1–8, lenses; PBS1/2, polarization beam splitters; BS1–4, intensity beam splitters; M1–6, mirrors; QW1–3, quarter-wave plates; A1–2, diaphragms; P1–2, polarizers; WFS, wavefront sensor.

components of SoP. According to the property of PBS, the reflected and transmitted lights has vertical linear SoP and horizontal linear SoP respectively, they will transmit the cyclic RSI system along anticlockwise direction (i.e. PBS1 → L5 → M1 → M2 → L6 → PBS1) and clockwise direction (i.e. PBS1 → L6 → M2 → M1 → L5 → PBS1) respectively and are guided into FCCPS system. These two beams are magnified and de-magnified due to the different focal lengths of lenses L5 and L6.

The complex amplitude of the incident light $E_0(x, y)$ can be presented as

$$E_0(x,y) = A_0(x,y) \exp\left[-i\varphi_0(x,y)\right] \tag{1}$$

where $A_0(x, y)$ and $\varphi_0(x, y)$ are the amplitude distribution and the phase distribution (i.e. wavefront) respectively, and (x, y) represents the spatial coordinates of amplitude and phase of the complex amplitude.

Assuming the focal length of L6 (i.e. f_6) larger than the focal length of L5 (i.e. f_5), the radial shearing ratio $s = f_6/f_5$ is larger than 1. Then $E_1(x, y)$ and $E_2(x, y)$, which are the complex amplitudes of two exiting beams from the cyclic RSI, can be presented by

$$\begin{cases} E_1(x,y) = A_0(x/s,y/s) \exp\left[-i\varphi_0(x/s,y/s)\right] \\ \qquad\quad = A_1(x,y) \exp\left[-i\varphi_1(x,y)\right] \\ E_2(x,y) = A_0(xs,ys) \exp\left[-i\varphi_0(xs,ys)\right] \\ \qquad\quad = A_2(x,y) \exp\left[-i\varphi_2(x,y)\right] \end{cases} \tag{2}$$

where $A_{1/2}(x, y)$ present the amplitude distributions of magnified and de-magnified beams respectively; $\varphi_1(x, y)$, $\Delta\varphi_2(x, y)$ presents the phase distributions of magnified and de-magnified beams respectively. Their definitions are shown as

$$\begin{cases} A_1(x,y) = A_0(x/s, y/s) \\ \varphi_1(x,y) = \varphi_0(x/s, y/s) \\ A_2(x,y) = A_0(xs, ys), \\ \varphi_2(x,y) = \varphi_0(xs, ys) \end{cases} \tag{3}$$

The aperture size of incident laser beam is limited as D by A1, and the corresponding beam size of exiting beams from cyclic RSI will be Ds and D/s respectively. The beam size is filtered again as same with their common area by A2 before they are introduced into FCCPS, as shown in **Figure 1**.

The FCPPS will generate the desired phase shifts of $\pi/2$ between each generated interferograms. Firstly, two beams, which generated from the cyclic RSI, are equally divided into two channels (i.e. channel a and channel b, shown in **Figure 1**) by the BS3. QW1 (angle distance of 0° from its fast axis to horizontal direction) and QW2 (angle distance of 45° from its fast axis to horizontal direction) are placed in channel a. QW1 generates a $\lambda/4$ phase delay between the Beam1 and the Beam2, and QW2 converts two beams into circularly polarized lights with levorotation and dextrorotation respectively. QW3 is placed into the channel b, and its fast axis keeps accordance to QW2. Another two circularly polarized beams with levorotation and dextrorotation are generated. The beams of channel a and b is split into four beam pairs by PBS2, i.e. a1, a2, b1 and b2 respectively, and it will introduces $\lambda/2$ phase delay into between channel 1 and 2. Four beam pairs are spatial arranged properly by mirrors M5 and M6 and beam splitter BS4, and they are projected onto the photosensitive plane of a CCD camera by the relay optics system composed of lenses L7 and L8. Finally, four interferograms are detected and recorded by the CCD camera.

The basic principle of the spatial phase-shifting can be explained by Jones formulas. The Jones matrices for a horizontal linear polarizer P_0, a vertical linear polarizer P_{90}, and a quarter-wave plate with horizontal fast axis Q_0, and 45° fast axis Q_{45}, are respectively

$$P_0 = \begin{bmatrix} 1 & 0 \\ 0 & 0 \end{bmatrix}, P_{90} = \begin{bmatrix} 0 & 0 \\ 0 & 1 \end{bmatrix}, Q_0 = \begin{bmatrix} 1 & 0 \\ 0 & -i \end{bmatrix}, Q_{45} = \frac{1}{\sqrt{2}}\begin{bmatrix} 1 & i \\ i & 1 \end{bmatrix} \tag{4}$$

The Jones matrix in the polarization state for each of the four channels can be represented by

$$a1 = P_0 Q_{45} Q_0 = \frac{1}{\sqrt{2}}\begin{bmatrix} 1 & 1 \\ 0 & 0 \end{bmatrix}, a2 = P_{90} Q_{45} Q_0 = \frac{1}{\sqrt{2}}\begin{bmatrix} 0 & 0 \\ i & -i \end{bmatrix},$$

$$b1 = P_0 Q_{45} = \frac{1}{\sqrt{2}}\begin{bmatrix} 1 & i \\ 0 & 0 \end{bmatrix}, b2 = P_{90} Q_{45} = \frac{1}{\sqrt{2}}\begin{bmatrix} 0 & 0 \\ i & 1 \end{bmatrix} \tag{5}$$

From Eq. (5), 0, 90, 180 and 270° phase shifting have been generated between each beam pair, which are the a1, b1, a2 and b2 respectively.

Wavefront difference $\Delta\varphi(x, y)$, which presents the difference between wavefront of Beam1 and Beam2 in their interference zone can be written as

$$\Delta\varphi(x,y) = \varphi_2(x,y) - \varphi_1(x,y) = \varphi_0(xs, ys) - \varphi_0(x/s, y/s) \tag{6}$$

The interference intensity of four interferograms, which are expressed by I_{a1}, I_{b1}, I_{a2} and I_{b2} respectively, can be represented by

$$
\begin{aligned}
I_{a1} &= A_1^2/2 + A_2^2/2 + A_1 A_2 \cos(\Delta\varphi) \\
I_{b1} &= A_1^2/2 + A_2^2/2 + A_1 A_2 \cos(\Delta\varphi + \pi/2) \\
I_{a2} &= A_1^2/2 + A_2^2/2 + A_1 A_2 \cos(\Delta\varphi + \pi) \\
I_{b2} &= A_1^2/2 + A_2^2/2 + A_1 A_2 \cos(\Delta\varphi + 3\pi/2)
\end{aligned}
\tag{7}
$$

where I_{ai}, I_{bi}, A_i and $\Delta\varphi$ are the abbreviations of $I_{ai}(x, y)$, $I_{bi}(x, y)$, $A_i(x, y)$ and $\Delta\varphi(x, y)$, here i = 1,2.

Thus the wavefront difference $\Delta\varphi(x, y)$ can be calculated by classic four-frame phase shifting algorithm, which given by

$$
\Delta\varphi(x, y) = \tan^{-1}\left[\frac{I_{b2}(x,y) - I_{b1}(x,y)}{I_{a1}(x,y) - I_{a2}(x,y)}\right]
\tag{8}
$$

Then, a suitable phase unwrapping algorithm is employed to acquire the absolute wavefront difference distribution.

2.2 Experimental results and analysis

As a comparison, a wavefront simulator (WS), which is composed mainly of an electrically addressed phase-only liquid crystal spatial light modulator (LC SLM), is adopt in experimental system to generate the candidate wavefront, and it will be measured by both a Hartmann-Shack wavefront sensor and the described RSI. For achieving this goal, the LC SLM should be adjusted in a phase-only modulation mode by keeping accordance of polarization state between polarizer and LC SLM. The generated wavefront by WS is measured separately, and compare with that obtained by the proposed RSI. The lenses L3 and L4 placed in HS WFS system relay the LC SLM to the HS WFS. The experiment is performed with a He-Ne laser, and its wavelength λ = 632.8 nm. The focal length of Lens1 and Lens2 are 250 mm and 300 mm respectively. Four interferograms are detected by one 8 bit, 576 × 768 pixels CCD camera. The full resolution of HS WFS is 32 × 32, and the aberrated wavefront are generated by a 512 × 512 pixel LC SLM.

Figure 2 shows the practical experimental setup of the proposed RSI. In experiments, we find the best angle for acquiring highest fringe visibility firstly. Then the LC SLM is controlled to generate a random aberration, which is a combination of 45-limit order Zernike polynomials. Four fringe patterns were detected simultaneously by the CCD camera, and they are shown in **Figure 3**.

The wrapped wavefront difference $\Delta\varphi(x, y)$ can be calculated according to Eq. (8). The unwrapped result is also shown in **Figure 4(b)**. A modal wavefront reconstruction method is employed to reconstruct the wavefront under test from the unwrapped wavefront differences. The RMS and the PV of the reconstructed wavefront are 0.4753λ and 3.3222λ, respectively, and here RMS and PV represent the root-mean-square value and peak-to-valley value of the wavefront under test. When we normalize the RMS value of each order Zernike polynomial to 1.0λ, the Zernike polynomial coefficients of the wavefront under test can be obtained by using the least square method, and it is shown in **Figure 5(b)**.

The same aberrated wavefront also detected by HS WFS separately. A spot array is detected is split into HS WFS, and the corresponding gradient distributions along horizontal and vertical directions can be calculated. Finally the wavefront under test was reconstructed again by using a similar modal reconstruction method. **Figure 6(a)**
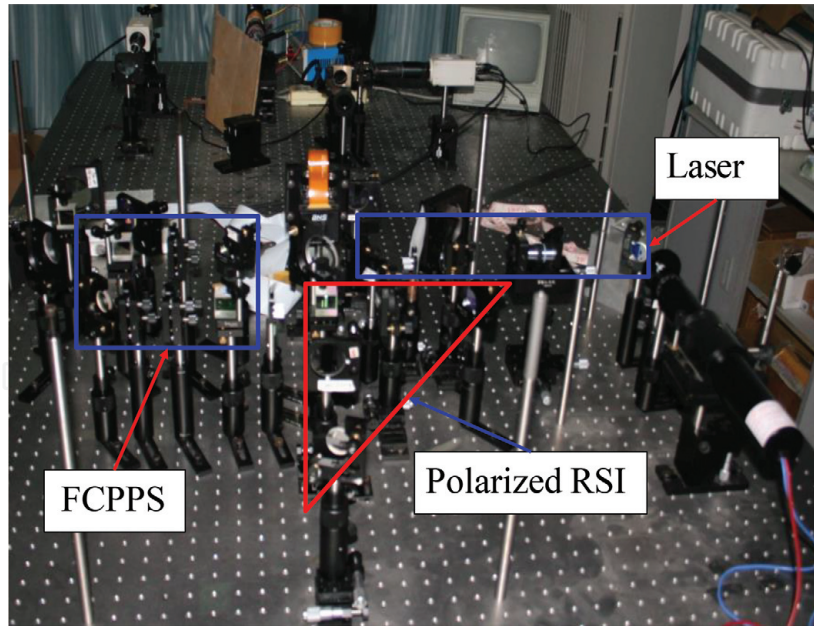
Figure 2.
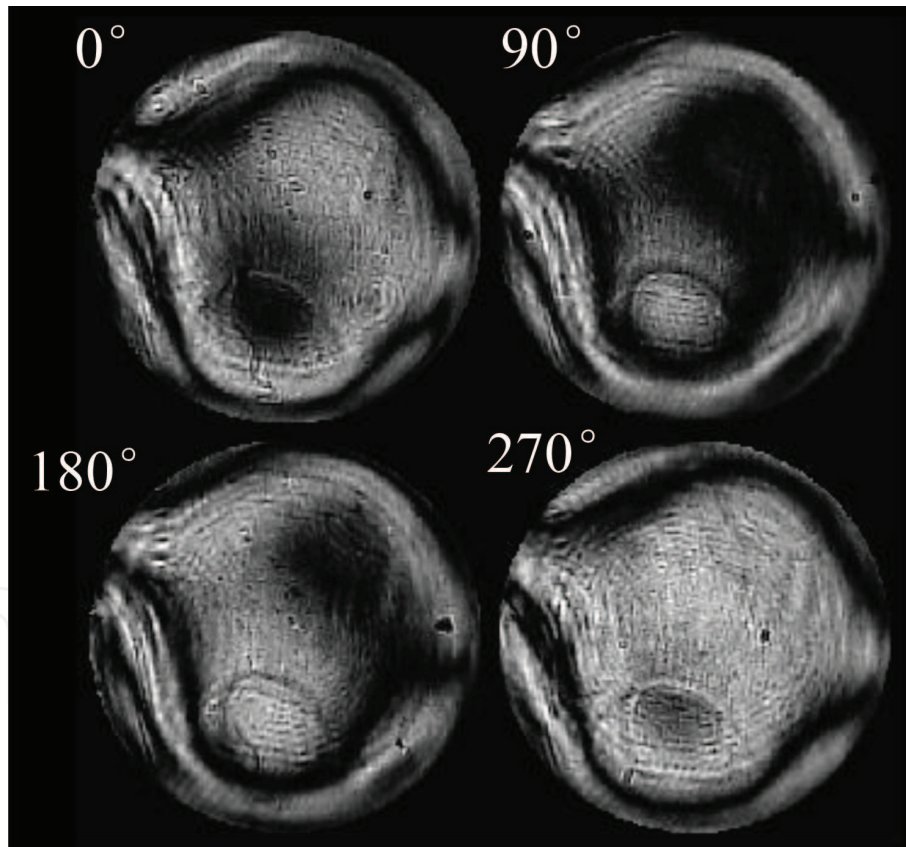*Experimental setup of the proposed RSI.*

Figure 3.
Interferograms recorded by the experimental setup.

shows the reconstructed result, and the RMS and PV are 0.4798λ and 3.5953λ, respectively. The residual error, which is the difference between these two wavefront under test measured by the proposed RSI and the HS WFS, is also drawn in **Figure 6(b)**, and the corresponding RMS and PV are 0.0348λ and 0.3149λ, respectively.

From **Figure 6**, a small residual error is obtained, and the result measured by the proposed RSI keeping accordance with HS WFS. The difference is mainly due
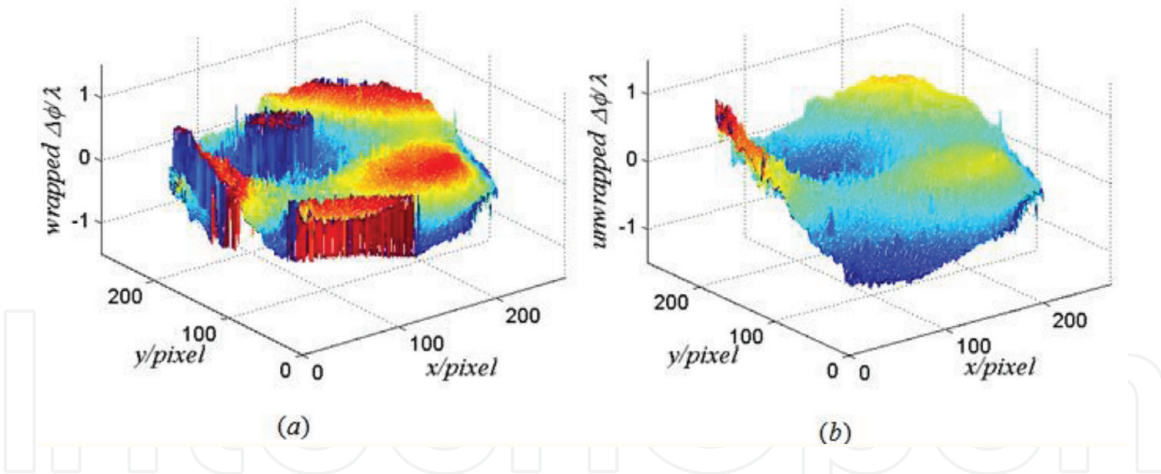
Figure 4.
*The wavefront difference calculated from the four interferograms (shown in **Figure 3**). (a) The wrapped wavefront difference and (b) the unwrapped wavefront difference.*
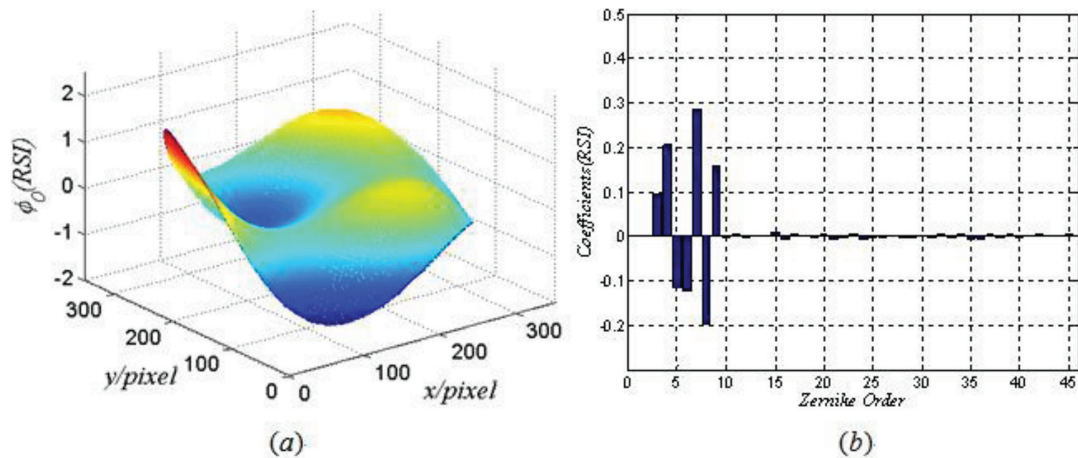

Figure 5.
*The wavefront under test measured by the proposed RSI. (a) The 3D plot of the wavefront under test reconstructed from the wavefront difference shown in **Figure 4(b)** and (b) the coefficients of the first 45 order Zernike polynomials.*
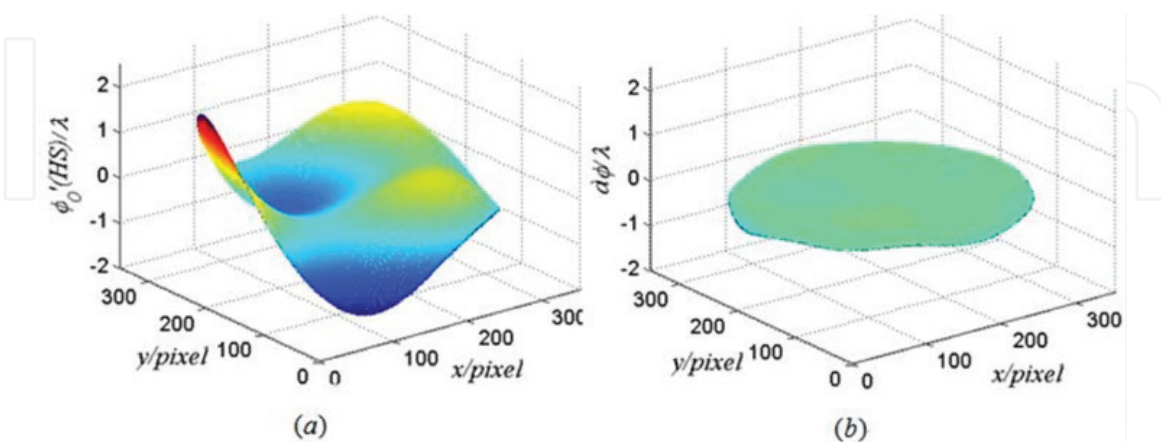

Figure 6.
The measured results of HS WFS and the residual error. (a) Experimental result measured by HS WFS (RMS and PV are 0.4798λ and 3.5953λ respectively) and (b) residual errors between wavefront measured by RSI and HS-WFS (RMS and PV are 0.0348λ and 0.3149λ respectively).

to the detecting noise of the CCD camera and the grating effect of the LC SLM. Better results would be acquired when a high performance CCD camera and a continuous surface wavefront simulator are used.
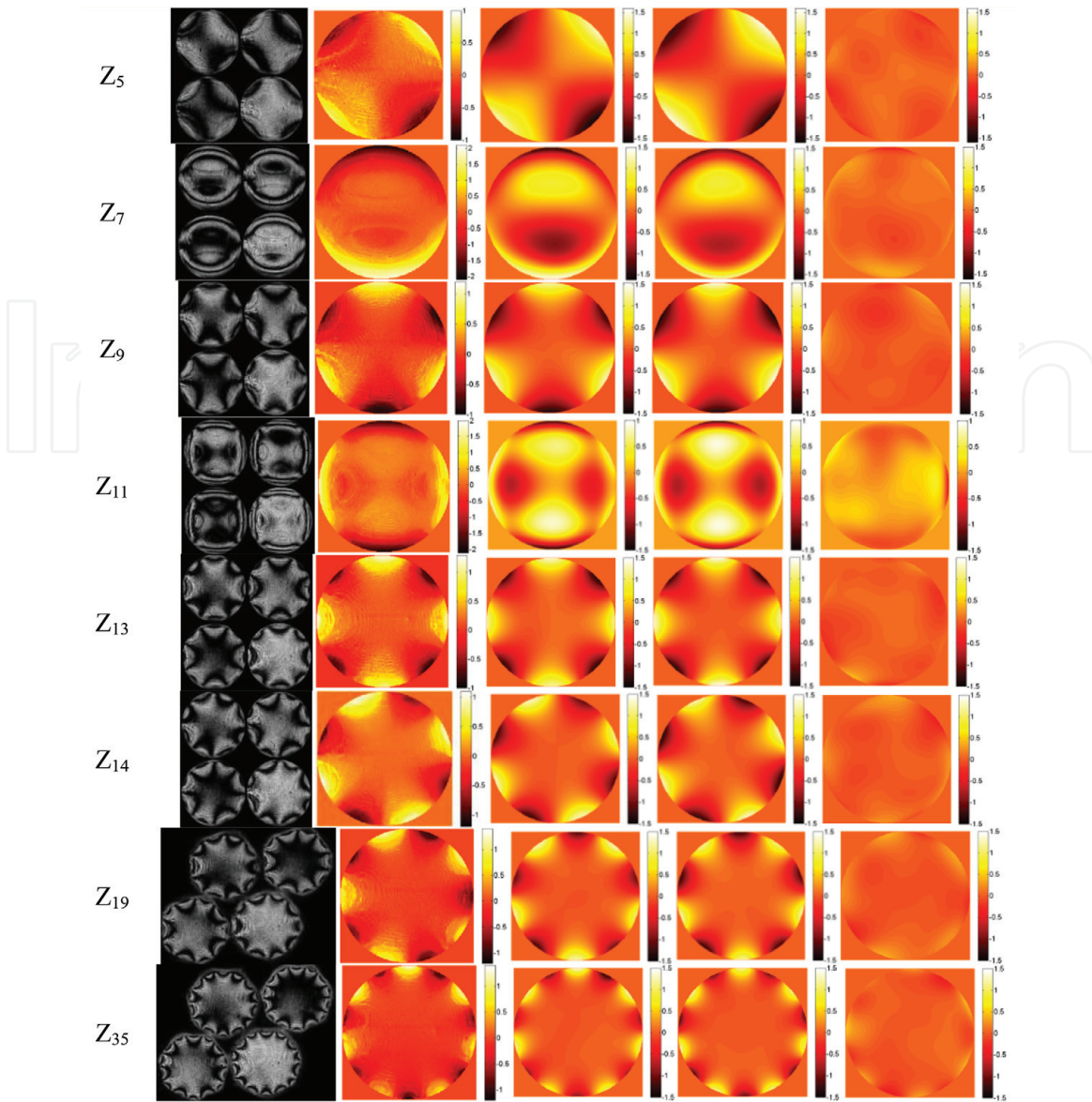
Figure 7.
Experimental results when the LC SLM generates some wavefront under test with single Zernike polynomial.
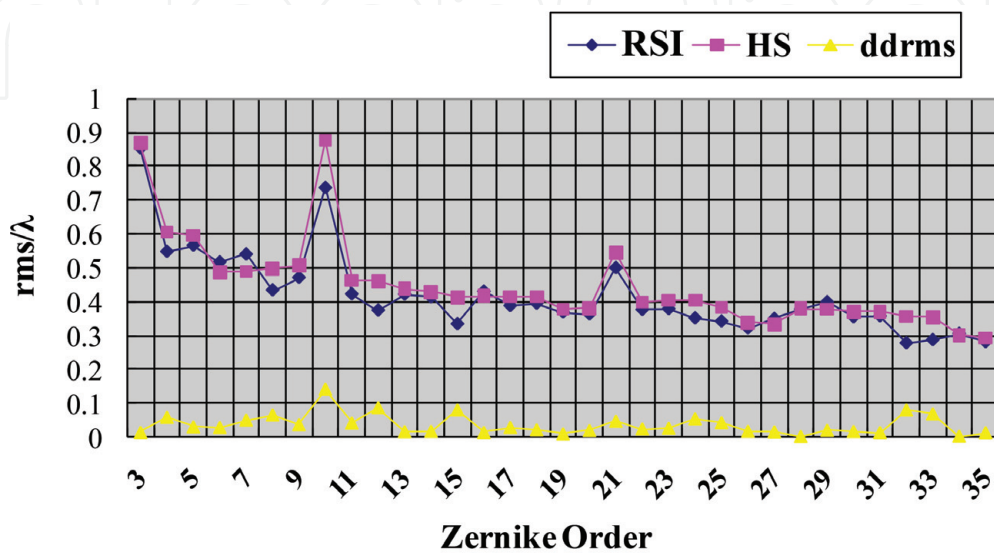

Figure 8.
Experimental results when the LC SLM generates some wavefront under test with single Zernike polynomial.

Figure 7 gives the other experimental results when the LC SLM generates some wavefront under test with single Zernike polynomial. **Figure 8** shows the statistic results of RMS and PV of 3–35 order Zernike polynomials measured by the proposed RSI and HS WFS.

3. Compact RSI based on micro-retarder array

In RSIs, complex configuration limits the measurement accuracy, system stability, and its application. Apparently, it is highly desirable to design compact one-shot vibration-insensitive RSIs. In this part, we will introduce a compact RSI based on pixelated micro-retarder-array (MRA).

3.1 Design and theory of the compact RSI

The basic concept and the schematic layout of the new compact RSI based on MRA are shown in **Figure 9**. The cyclic RSI is a Keplerian telescope system, which is same as the counterpart of **Figure 1**. The complex amplitude $E_0(x, y)$ can also be presented by Eq. (1). The half-wave retarder (HWR) is to adjust the polarization of the introduced light beam. Let θ as the angle between the polarization orientation of the introduced beam and the fast axis of the HWR. The polarization of the beam will be rotated by 2θ after passing through the HWR. The PBS splits the incident light into two beams with perpendicular polarization. The complex amplitude distributions of the new beam are generated when they pass through L1 and L2 and L2 and L1, respectively.

Figure 10 illustrates polarization conversion and complex amplitude after passing through different optical elements. $E_0(x, y)$ presents the optical field of the incident beam, and the variable α presents the angle of its SoP relative to x axis (i.e. horizontal direction). $E'_0(x, y)$ presents the complex amplitude of the exiting beam from HWR. The fast axis of HWR is presented by the dashed line. The complex amplitudes of reflection beam and transmission beam after passing through PBS can be presented as

$$E_p(x,y) = E'_0(x,y) \cos(\alpha - 2\theta), \quad E_s(x,y) = E'_0(x,y) \sin(\alpha - 2\theta) \qquad (9)$$

In fact the $E'_0(x, y)$ can be treated same as the $E_0(x, y)$ in scalar field because they have the same amplitude and phase distribution when they passing through HWR, which just change the SoP of the incident beam under different fast axis. Similar to the cyclic RSI in **Figure 1**, there are also two beams, i.e. magnified (i.e. $E_{\exp}(x, y)$)
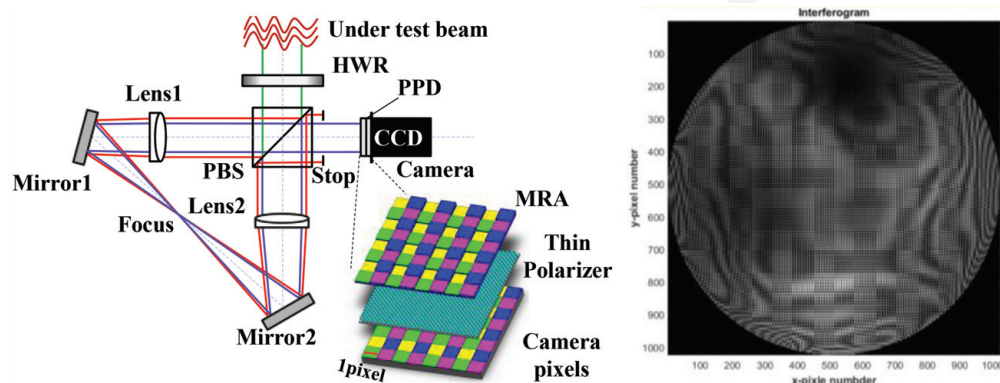

Figure 9.
Concept design of the proposed compact RSI. PPD, pixelated polarization device; HWR, half-wave retarder; PBS, polarized beam splitter; MRA, micro-retarder array.
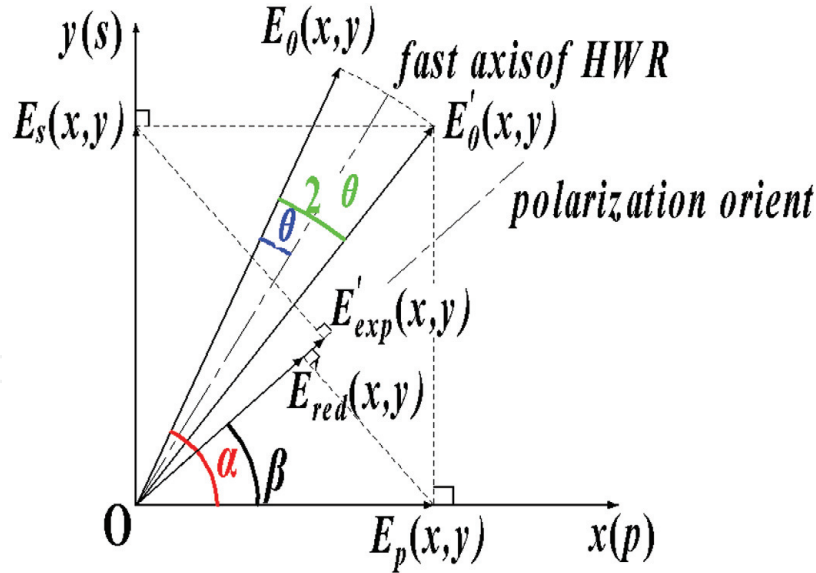
Figure 10.
Sketch map of SoPs conversion.

and de-magnified (i.e. $E_{\text{red}}(x,y)$) beams, are generated by the cyclic RSI, and they can be presented by

$$
\begin{aligned}
E_{\exp}(x,y) &= E_s(x/s, y/s)/s \\
E_{red}(x,y) &= sE_p(xs, ys)
\end{aligned}
\tag{10}
$$

Finally the complex amplitude distribution of expanded and reduced beams can be presented as

$$
\begin{aligned}
E_{\exp}(x,y) &= \frac{1}{s}A_0'\left(\frac{x}{s},\frac{y}{s}\right)\exp\left[-j\varphi_0\left(\frac{x}{s},\frac{y}{s}\right)\right] \\
E_{red}(x,y) &= sA_0''(xs, ys)\exp\left[-j\varphi_0(xs, ys)\right]
\end{aligned}
\tag{11}
$$

where $A_0'(x,y) = A_0(x,y)\sin(\alpha - 2\theta)$, and $A_0''(x,y) = A_0(x,y)\cos(\alpha - 2\theta)$.

Then the expanded beam and reduced beam with orthogonal polarization are introduced into the proposed phase-shifter, which consists of a micro-retarder array (MRA) and a piece of thin polarizer. Each macro pixel of MRA is composed of four neighboring pixels with different-thickness (as shown in **Figure 11(a)**). The MRA is made by a slice of birefringent crystal, and it can be quartz, calcite or the other kind of optical birefringent material. The fast axis of the selected bire-fringent crystal should be along or orthometric with x axis (i.e. horizontal direc-tion) for keeping polarization status of incident light from changes when different phase-shifts are introduced. The schematic diagram of the MRA is drawn in **Figure 11**, and the basic principle of phase delay between two radial shearing beams is also introduced.

Pixel size of the MRA should be kept accordance with the pixel size of camera, and they should be integrated onto the photosensitive plane of the camera pixel by pixel. Here a negative single axis birefringent crystal is assumed, and let the fast axis of it along vertical direction. Thus the phase-delays of the four neighboring pixels is

$$
\Delta\delta_i = (n_o - n_e)d_i \cdot 2\pi/\lambda, \, i = 1, 2, 3, 4
\tag{12}
$$

where λ is the center wavelength of light, and i is the sequence number of the four neighboring pixels.
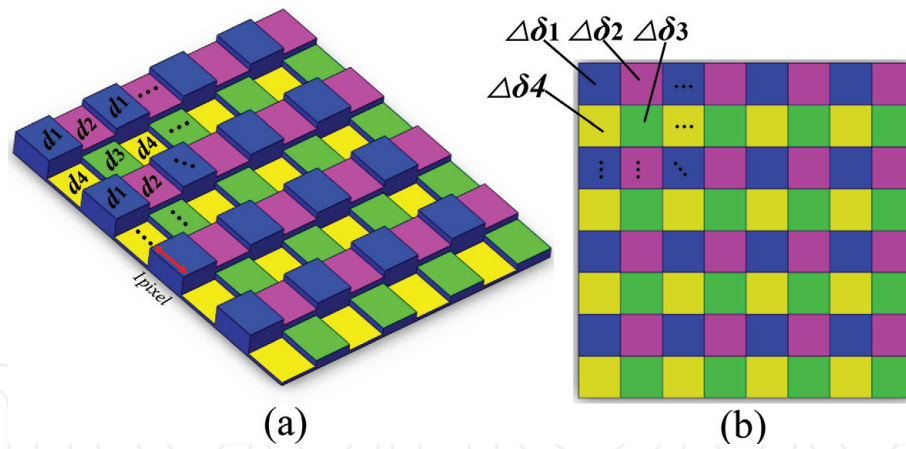
Figure 11.
Schematic diagram of the MRA. (a) MRA composed of units with different-thickness pixels made by a slice of birefringence crystal, and (b) the phase delay of each pixel. d_1–d_4: thickness at four neighboring pixels, $\Delta\delta1$–$\Delta\delta4$: phase-shifting between s- and p-light for four neighboring pixels.

When these two beams exiting from the cyclic RSI transmit through MRA, Eq. (11) at each pixel is changed as

$$E_{\exp,i}(x,y) = A'_0(x/s, y/s) \exp\left[-j(\varphi_0(x/s, y/s) + \delta_i + \Delta\delta_i)\right]/s$$
$$E_{red,i}(x,y) = sA''_0(xs, ys) \exp\left[-j(\varphi_0(xs, ys) + \delta_i)\right] \tag{13}$$

where δ_i are the phase-shifts when the o-light transmits through MRA. After passing through the thin polarizer, Eq. (13) can be rewritten by

$$E'_{\exp,i}(x,y) = E_{\exp,i}(x,y) \sin\beta$$
$$E'_{red,i}(x,y) = E_{con,i}(x,y) \cos\beta \tag{14}$$

here β presents the filtering angle of the thin polarizer relative to horizontal direction, as shown in **Figure 10**.

After passing through the thin polarizer, the beams will be interference with each other on the pixels of the camera, and the intensity at four adjacent pixels can be represented as

$$I_i(x,y) = \left|E'_{\exp,i}(x,y)\right|^2 + \left|E'_{red,i}(x,y)\right|^2 + 2\left|E'_{\exp,i}(x,y)\right|\left|E'_{red,i}(x,y)\right| \cos\left[\Delta\varphi(x,y) + \Delta\delta_i(x,y)\right]$$
$$= I_a(x,y) + I_b(x,y) + 2\sqrt{I_a(x,y)I_b(x,y)} \cos\left[\Delta\varphi(x,y) + \Delta\delta_i(x,y)\right] \tag{15}$$

where $\Delta\varphi(x,y)$ represents the mean phase difference between the beams at (x,y) position. x and y presents the center position of each macro-pixel.

Combining the Eqs. (11), (13)–(15), a new equation can be obtained as

$$I_a(x,y) = I_0\left(\frac{x}{s}, \frac{y}{s}\right) \sin^2\beta \sin^2(\alpha - 2\theta)/s^2,$$
$$I_b(x,y) = s^2 I_0(xs, ys) \cos^2\beta \cos^2(\alpha - 2\theta)$$
$$\Delta\varphi(x,y) = \varphi_0(xs, ys) - \varphi_0\left(\frac{x}{s}, \frac{y}{s}\right), \tag{16}$$
$$I_0(x,y) = |E_0(x,y)|^2 = |A_0(x,y)|^2$$

Eq. (15) can be expressed in discrete form as

$$I_i(m,n) = I_a(m,n) + I_b(m,n) + 2\sqrt{I_a(m,n)I_b(m,n)}\cos\left[\Delta\varphi(m,n) + \Delta\delta_i(m,n)\right]$$
(17)

where (m,n) is a discrete form of (x,y), which presents the coordinate positions. Assuming the number of rows and columns of camera pixels are $2M_0$ and $2N_0$ respectively, the (m,n) should take a value from 1 to M_0 and 1 to N_0 respectively.

Then Eq. (17) can be rewritten as

$$I_i(m,n) = K(m,n) + L(m,n)\cos\left[\Delta\delta_i(m,n)\right] - R(m,n)\sin\left[\Delta\delta_i(m,n)\right]$$
(18)

where

$$K(m,n) = I_a(m,n) + I_b(m,n)$$

$$L(m,n) = 2\sqrt{I_a(m,n)I_b(m,n)}\cos\left[\Delta\varphi(m,n)\right]$$
(19)

$$R(m,n) = 2\sqrt{I_a(m,n)I_b(m,n)}\sin\left[\Delta\varphi(m,n)\right]$$

Eq. (19) can be expressed by matrix form, and it is

$$
\begin{bmatrix}
I_1(m,n) \\
I_2(m,n) \\
I_3(m,n) \\
I_4(m,n)
\end{bmatrix}
=
\begin{bmatrix}
1 & \cos\left[\Delta\delta_1(m,n)\right] & -\sin\left[\Delta\delta_1(m,n)\right] \\
1 & \cos\left[\Delta\delta_2(m,n)\right] & -\sin\left[\Delta\delta_2(m,n)\right] \\
1 & \cos\left[\Delta\delta_3(m,n)\right] & -\sin\left[\Delta\delta_3(m,n)\right] \\
1 & \cos\left[\Delta\delta_4(m,n)\right] & -\sin\left[\Delta\delta_4(m,n)\right]
\end{bmatrix}
\begin{bmatrix}
K(m,n) \\
L(m,n) \\
R(m,n)
\end{bmatrix}
$$
(20)

Thus

$$
\begin{bmatrix}
K(m,n) \\
L(m,n) \\
R(m,n)
\end{bmatrix}
=
\begin{bmatrix}
A_1(m,n) & B_1(m,n) & C_1(m,n) & D_1(m,n) \\
A_2(m,n) & B_2(m,n) & C_2(m,n) & D_2(m,n) \\
A_3(m,n) & B_3(m,n) & C_3(m,n) & D_3(m,n)
\end{bmatrix}
\begin{bmatrix}
I_1(m,n) \\
I_2(m,n) \\
I_3(m,n) \\
I_4(m,n)
\end{bmatrix}
$$
(21)

where

$$
\begin{bmatrix}
A_1(m,n) & B_1(m,n) & C_1(m,n) & D_1(m,n) \\
A_2(m,n) & B_2(m,n) & C_2(m,n) & D_2(m,n) \\
A_3(m,n) & B_3(m,n) & C_3(m,n) & D_3(m,n)
\end{bmatrix}
=
\begin{bmatrix}
1 & \cos\left[\Delta\delta_1(m,n)\right] & -\sin\left[\Delta\delta_1(m,n)\right] \\
1 & \cos\left[\Delta\delta_2(m,n)\right] & -\sin\left[\Delta\delta_2(m,n)\right] \\
1 & \cos\left[\Delta\delta_3(m,n)\right] & -\sin\left[\Delta\delta_3(m,n)\right] \\
1 & \cos\left[\Delta\delta_4(m,n)\right] & -\sin\left[\Delta\delta_4(m,n)\right]
\end{bmatrix}^{+}
$$
(22)

The matrix K, L and R can be solved for all units $M_0 \times N_0$ by

$$K = A_1. \times I_1 + B_1. \times I_2 + C_1. \times I_3 + D_1. \times I_4$$
$$L = A_2. \times I_1 + B_2. \times I_2 + C_2. \times I_3 + D_2. \times I_4$$
$$R = A_3. \times I_1 + B_3. \times I_2 + C_3. \times I_3 + D_3. \times I_4$$
(23)

For constant phase-shifts $\triangle\delta_1$–$\triangle\delta_4$, A_1–D_3 are constant coefficients that can be calculated by Eq. (22) or calibrated by only one time. They can be used to extract random phase delay when the matrix of Eq. (22) is reversible.

Combining Eqs. (19) and (23), the phase difference between two shearing beams can be presented as

$$\Delta\varphi(m,n) = \tan^{-1}[R(m,n)/L(m,n)] \qquad (24)$$

The wavefront under test $\varphi_0(x,y)$ can be reconstructed by Zernike mode [11] and iterative methods [30, 31].

The fringe visibility can be adjusted by changing the angle of HWR. Let ρ_0 as the mean power density of beam under test, the power density of the reduced beam ρ_p and the expanded beam ρ_s exiting the polarizer can be written by

$$\rho_p = \rho_0 \cos^2(\alpha - 2\theta) \cdot s^2 \cdot \cos^2\beta$$
$$\rho_s = \rho_0 \sin^2(\alpha - 2\theta)/s^2 \cdot \sin^2\beta \qquad (25)$$

For the best fringe visibility, ρ_p should be equal to ρ_s, and that means

$$\tan(\alpha - 2\theta)\tan\beta = s^2 \qquad (26)$$

Generally, for a certain RSI system, the shear ratio s and the angle β are constants, so the fringe visibility can be adjusted by change of θ according to the polarization angle α of the beam under test.

3.2 Validation by numeric analysis

In this part, numeric analysis is made for validating the feasibility of the proposed compact RSI. The systematic parameters are listed as follows: aperture size Φ = 5 mm, random polarization angle of beam under test α = 139°, wavelength λ = 632.8 nm, focal lengths of Lens1 f_1 = 50 mm, focal lengths of Lens2 f_2 = 60 mm, β = 45°. And calcite retarder is chosen with vertical fast axis and (n_e, n_o) = (1.4852, 1.6557), thickness of four pixels per unit are [0.0591, 0.1536, 0.3072, 0.4785] μm. The pixel size of 1024 × 1024 camera is 9.8 μm × 9.8 μm. For the proposed RSI, the phase-shifts at four adjacent pixels per unit are [0.6283, 1.6336, 3.2673, 5.0894] rad, and θ is 41.89° for acquiring the best fringe visibility.

The beam under test is generated with random complex amplitude, which are shown in **Figure 12(a)** and **(b)**, respectively. The interferogram generated by the proposed RSI is calculated from Eqs. (12), (15) and (16), as shown in **Figure 12(a)**. The matrix K, L and R are calculated by Eqs. (22) and (23). The wavefront difference between two shearing beams, as shown in **Figure 12(b)**, is extracted by Eq. (24).
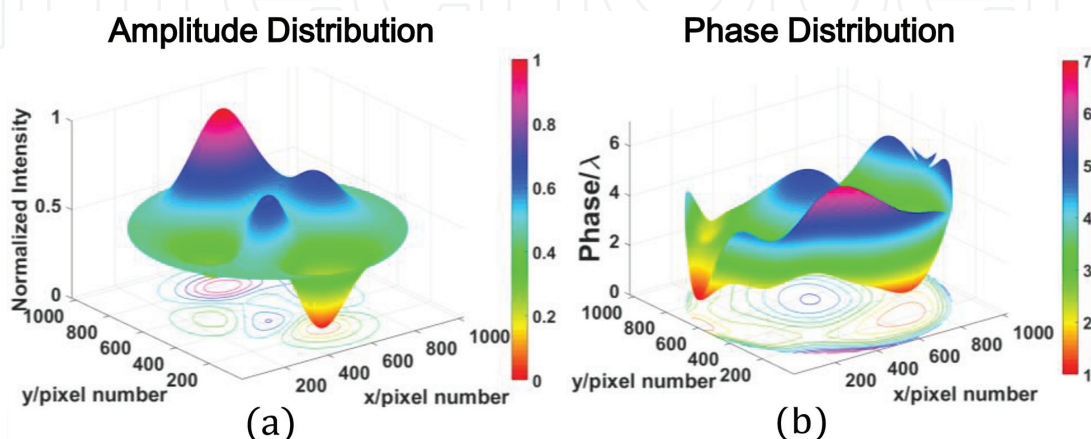

Figure 12.
Complex amplitude of the beam under test. (a) Random amplitude distribution generated by combination of 3-Gaussi functions, and (b) random phase distribution generated by combination of 65-limit Zernike polynomials (RMS = 0.975λ, PV = 5.736 λ).
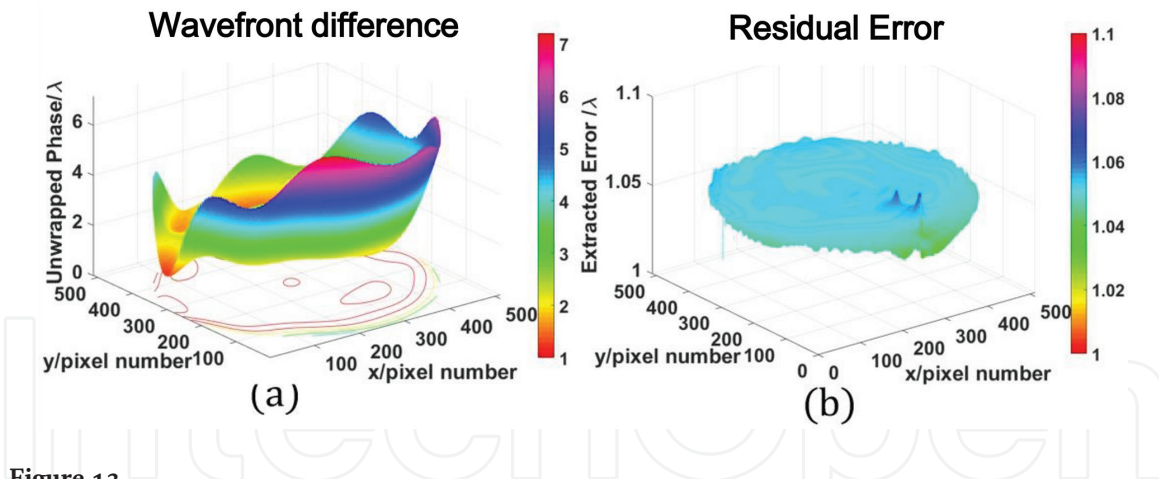
Figure 13.
The wavefront difference and its residual error relative to ideal value. (a) The unwrapped wavefront difference (RMS = 0.972λ), and (b) the error of the extracted wavefront difference (RMS = 0.002λ).
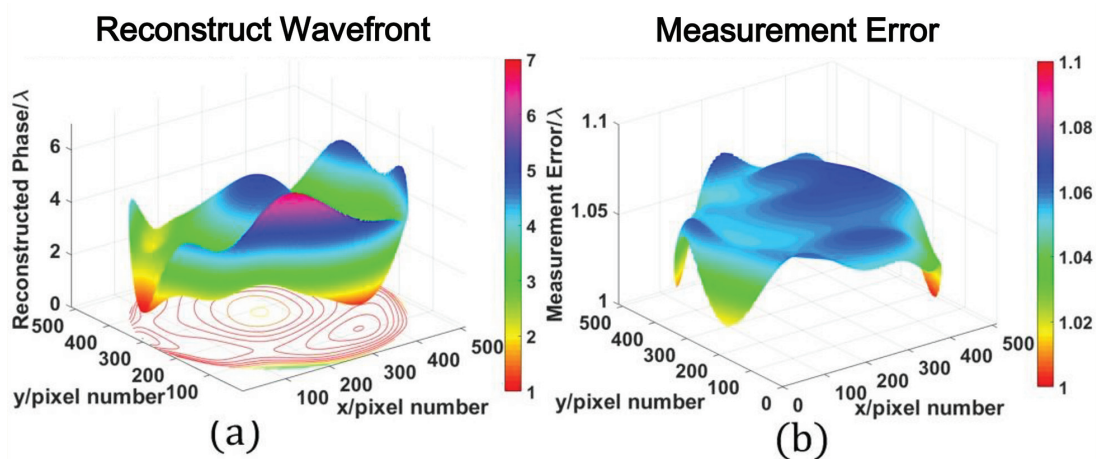

Figure 14.
The reconstruction result and the residual error. (a) The reconstruction result (RMS = 0.975λ), and (b) the residual error (RMS = 0.008λ).

Figure 13 shows the wavefront difference between two radial shearing beams and the deviation relative to the ideal wavefront difference. As seen from **Figure 13(b)**, the extracted error is less than 0.2%. The error is mainly caused by approximate treatment of intensity and phase values at four neighboring pixels. One should obtain a smaller deviation when a smoother intensity and phase distribution or large sampling number of camera is used.

Figure 14 shows the results of wavefront reconstruction. As seen from **Figure 14**, the RMS of the reconstructed wavefront is about 0.975λ, which is very close to the incident wavefront. The RMS of residual measurement error is about 0.008λ, which leads a relative deviation of 0.79%. In fact, if planar intensity amplitude and a smoother phase are employed in our numeric analysis, a better accuracy would be obtained based the method.

4. Modal method for reconstructing wavefront in RSI with or without later shear

In RSI no extra referencing planar wavefront but a magnified wavefront can be used as a reference. Thus the magnified and de-magnified beams should be aligned accurately avoiding wrong wavefront reconstruction. Unfortunately, two beams in

practical application are often misalignment, and a lateral shear is always exists in a RSI. Here we present a modal method to solve this problem.

4.1 Modal reconstruction method based Zernike polynomials

As shown in **Figure 15**, the wavefront difference at interference area can be described as

$$\Delta\varphi(x,y) = \varphi_1(x,y) - \varphi_2(x,y) \qquad (27)$$

The wavefront aberration $\varphi_1(x, y)$ is a de-magnified version of the wavefront under test $\varphi_0(x, y)$, and there no information is lost. So the wavefront aberration $\varphi_1(x, y)$ contains the same information with the wavefront under test $\varphi_0(x, y)$ if one normalize the diameter of the origin pupil and the de-magnified pupil. In other words, one can consider $\varphi_1(x, y)$ to be as the wavefront under test $\varphi_0(x, y)$. For simplicity, we define the interference area as $circle(d)$, and in this area two versions of wavefront under test can be expressed as

$$\begin{cases} \varphi_1(x,y) = \varphi_0(x,y) \\ \varphi_2(x,y) = \varphi_0(x/s^2, y/s^2) \end{cases}, \quad (x,y) \in circle(d) \qquad (28)$$

Eq. (28) is under an ideal alignment condition as shown in **Figure 15(a)**. However, in a practical RSI system lateral shear always exists and is inevitable. As shown in **Figure 15(b)**, the smaller circle denotes the de-magnified beam, and it also is the interference area, i.e. $circle(d)$. For convenience, the center of the contracted beam can be defined as the origin O of the Cartesian coordinate system, and the center position O′ of the magnified beam express the amount of lateral shear. Two variables, i.e. x_0 and y_0, are defined as the lateral shear at x direction and y direction respectively, and they can be calibrated by only one time measurement. Two versions of the wavefront under test can be rewritten as

$$\begin{cases} \varphi_1(x,y) = \varphi_0(x,y) \\ \varphi_2(x,y) = \varphi_0(x/s^2 - x_0, y/s^2 - y_0) \end{cases} \qquad (29)$$

Suppose that the $\varphi_0(x, y)$ can be described by a N-limited Zernike polynomials, and thus $\varphi_0(x, y)$ can be expressed as
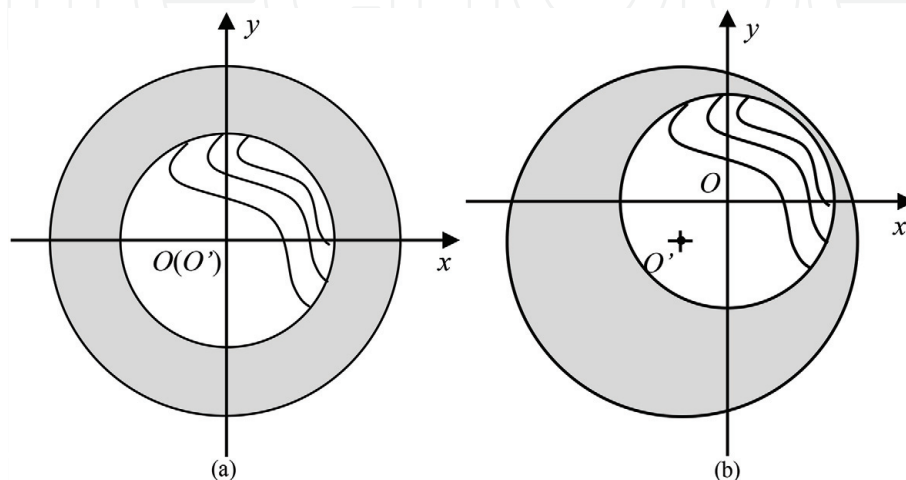

Figure 15.
Radial shearing interferogram without and with lateral shear. (a) Shearogram without lateral shear and (b) shearogram with lateral shear.

$$\varphi_0(x,y) = \sum_{k=0}^{N} a_k Z_k(x,y) \tag{30}$$

where $Z_k(x,y)$ is the kth order Zernike polynomial and a_k is the corresponding coefficient.

The magnified wavefront $\varphi_2(x,y)$ in $circle(d)$ can be written by

$$\varphi_2(x,y) = \sum_{k=0}^{N} a_k P_k(x,y) \tag{31}$$

where $P_k(x,y)$ is a portion of Zernike polynomials $Z_k^D(x,y)$ in the expanded beam area (denoted as $circle(D)$), i.e. $P_k(x,y) = Z_k^D(x,y)$, $(x,y) \in circle(d)$.

According to the reference [32], provided an N-limited Zernike description of a wavefront on a large pupil, any circular portion inside it can be described by another Zernike ensemble, limited to the same N. So the function $P_k(x,y)$ can be expressed by

$$P_k(x,y) = \sum_{j=0}^{k} b_j^k Z_j(x,y) \tag{32}$$

Put the Eqs. (30)–(32) into Eq. (2), a new equation is generated, and it is

$$\Delta\varphi(x,y) = \sum_{k=0}^{N} a_k Z_k(x,y) - \sum_{k=0}^{N} a_k \left[\sum_{j=0}^{k} b_j^k Z_j(x,y) \right] \tag{33}$$

Eq. (33) describes the relationship between the wavefront difference and the Zernike polynomials. However, it is also indirect and not clear. Actually, Eq. (33) can be rewrite in its matrix form, and it is expressed by

$$\Delta\varphi = [a_1 \cdots a_k \cdots a_N] \left\{ \begin{bmatrix} 1 & & & & \\ & \ddots & & & \\ & & 1 & & \\ & & & \ddots & \\ & & & & 1 \end{bmatrix} - \begin{bmatrix} b_1^1 & & & \\ \vdots & \ddots & & \\ b_1^k & \cdots & b_k^k & \\ \vdots & \vdots & \vdots & \ddots \\ b_1^N & \cdots & b_k^N & \cdots & b_N^N \end{bmatrix} \right\} \begin{bmatrix} Z_1 \\ \vdots \\ Z_k \\ \vdots \\ Z_N \end{bmatrix} \tag{34}$$

where $\Delta\varphi$ and Z_k are the compact form of matrix formalism of $\Delta\varphi(x,y)$ and $Z_k(x,y)$, respectively.

Eq. (34) can be simplified as

$$\Delta\varphi = \mathbf{ABZ} \tag{35}$$

where $\mathbf{A} = \{a_1, ..., a_k, ..., a_N\}$ is a coefficient vector of the wavefront under test; $\mathbf{Z} = \{Z_1, ..., Z_k, ..., Z_N\}^T$ is a column vector which is composed by a set of Zernike polynomials; $\mathbf{B}$ is a coefficient matrix, and it is

$$\mathbf{B} = \begin{bmatrix} 1 - b_1^1 & & & \\ \vdots & \ddots & & \\ -b_1^k & \cdots & 1 - b_k^k & \\ \vdots & \vdots & \vdots & \ddots \\ -b_1^N & \cdots & -b_k^N & \cdots & 1 - b_N^N \end{bmatrix} \tag{36}$$

On the other hand, the wavefront difference $\Delta\varphi(x, y)$ can be decomposed into a linear combination of the N-limited Zernike polynomials, and it is shown by

$$\Delta\varphi = \mathbf{CZ} \tag{37}$$

where $\mathbf{C} = \{c_1, ..., c_k, ..., c_N\}$ is the vector of coefficient.

There has only one unique decomposed result of Eq. (37) because the Zernike polynomials is orthogonal each other, and the solve can be presented as

$$\mathbf{C} = \mathbf{AB} \tag{38}$$

We can get

$$\mathbf{A} = \mathbf{CB}^+ \tag{39}$$

where $\mathbf{B}^+$ is the generalized inverse of the matrix $\mathbf{B}$.

The coefficient vector $\mathbf{C}$ can be calculated directly from Eq. (37), and the coefficient vector $\mathbf{A}$ can be determined by the matrix $\mathbf{B}$ finally. In fact, the matrix B can be determined beforehand by a numerical calculation or a calibration process for a certain radial ratio s and lateral shear x_0 and y_0. Then the wavefront difference $\Delta\varphi(x, y)$ can be expressed by a set of Zernike polynomials, and the corresponding coefficient vector $\mathbf{C}$ is calculated. Finally, the coefficient vector $\mathbf{A}$ can be determined by only one time matrix operation, and then the wavefront under test is reconstructed.

4.2 Numeric analysis

A random phase distribution is generated as wavefront under test for validating the proposed modal reconstruction method. A 45-limit Zernike polynomials are used, and the full resolution is 256×256. 1.2 of radial shear ratio s is assumed in a RSI, and $\eta_x = 10\%$ and $\eta_y = -18\%$ of relative lateral shear at x direction and at y direction respectively are used in our numeric analysis.

Here $\varphi_0(x, y)$ is presented by a random composition of 45-limited Zernike polynomials. Two variables, σ_{rms} and σ_{pv}, are used to express the root-mean-square (RMS) and peak-to-valley (PV) of the wavefront respectively. The 3D-plot of the simulated random wavefront $\varphi_0(x, y)$ is shown in **Figure 16(a)**. The RMS and PTV of the simulated wavefront under test are 2.000λ and 12.285λ respectively, where λ
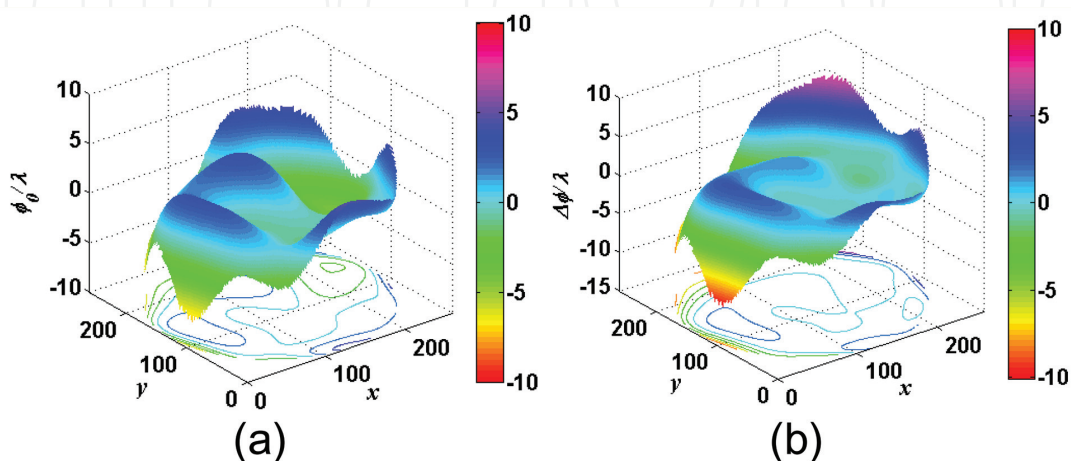

Figure 16.
Wavefront under test and the corresponding wavefront difference. (a) Random wavefront under test $\varphi_o(x, y)$ and (b) The wavefront difference $\Delta\varphi(x, y)$ calculated from $\varphi_o(x, y)$; the RMS and PTV of $\Delta\varphi(x, y)$ are 2.091λ and 18.057λ respectively.
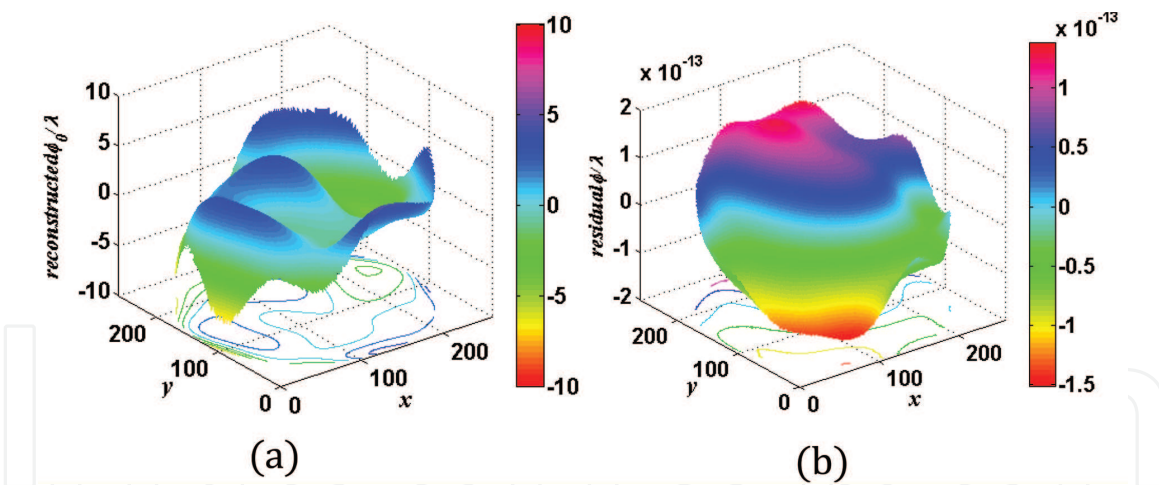
Figure 17.
Wavefront reconstruction and the corresponding residual error. (a) The reconstructed wavefront under test by substituting the vector A into Eq. (30) and (b) the residual error between the origin wavefront and the reconstructed wavefront.

is the wavelength of laser. According to the radial shear ratio s and the relative lateral shear η_x and η_y, the wavefront difference $\Delta\varphi(x, y)$ can be calculated easily, and it is shown in **Figure 16(b)**.

The coefficient matrix **B** can be calculated from Eqs. (32)–(36). According to the description of Eq. (39), the coefficient vector **A** is obtained. By applying Eq. (30), the wavefront of incident light can be reconstructed, and it is drawn in **Figure 17 (a)**. **Figure 17(b)** shows the residual error of wavefront reconstruction, and its corresponding RMS and PV are $7.003 \times 10^{-14}\lambda$ and $2.896 \times 10^{-13}\lambda$ respectively.

5. Conclusion

In this chapter, we have introduced briefly the history of RSI and the recent development. Two kinds of simultaneous RSI are also described in deep, including RSI based on simultaneous polarization phase-shifter and a new compact RSI based on micro-retarder array. Comparatively, the former one is suitable for wavefront measurements and diagnosing dynamic measurements, but its complex configuration limits the system stability, measurement accuracy and therefore its application. The new compact RSI based on micro-retarder array has several obvious advantages such as high-speed, high accuracy, vibration immunity, and compact size and so on, and it should be a kind of promising RSI in future. Complex extraction algorithm is another main barrier influencing the development of RSI. In this chapter a simple and useful modal reconstruction method is also given to extract the wavefront under test from the radial shearograms with or without lateral shear. Comparing with the previous method, the modal wavefront reconstruction method reduces effectively the noise accumulation and has good error propagation property. It is based on Zernike polynomials and its matrix formalism, and it should lead to an easier implementation in some practical situations.

Acknowledgements

Funding

Author details

Naiting Gu[1]* and Qun Luo[2]

1 Institute of Optics and Electronics, Chinese Academy of Sciences, Chengdu, China

2 National Key Laboratory of Science and Technology on Blind Signal Processing, Chengdu, China

*Address all correspondence to: gnt7328@163.com

IntechOpen

References

[1] Hariharan P, Sen D. Radial shearing interferometer. Journal of Scientific Instruments. 1961;**38**:428-432. DOI: 10.1088/0950-7671/38/11/305

[2] Liu D, Yang Y, Shen Y. System optimization of radial shearing interferometer for aspheric testing. Proceedings of SPIE. 2007;**6834**: 68340U-1-8. DOI: 10.1117/12.760132

[3] Wang M, Zhang B, Shouping N. Radial shearing interferometer for aspheric surface testing. Proceedings of SPIE. 2002;**4927**:673-676. DOI: 10.1117/12.471690

[4] Kohno T, Matsumoto D, Yazawa T. Radial shearing interferometer for in-process measurement of diamond turning. Proceedings of SPIE. 1997;**3173**: 280-285. DOI: 10.1117/12.294519

[5] Kowalik W, Garncarz B, Kasprzak H. Corneal topography measurement by means of radial shearing interference: Part I—Theoretical consideration. Optik. 2002;**113**:39-45. DOI: 10.1078/0030-4026-00113

[6] Kowalik W, Garncarz B, Kasprzak H. Corneal topography measurement by means of radial shearing interference: Part II—experiment results. Optik. 2002;**113**:46-50. DOI: 10.1078/0030-4026-00112

[7] Kowalik W, Garncarz B, Kasprzak H. Corneal topography measurement by means of radial shearing interference: Part III—measurement errors. Optik. 2003;**114**:199-206. DOI: 10.1078/0030-4026-00247

[8] Gu N, Huang L, Yang Z. Changhui Rao: A single-shot common-path phase-stepping radial shearing interferometer for wavefront measurements. Optics Express. 2011;**19**:4703-4713. DOI: 10.1364/OE.19.004703

[9] Cheung D, Barnes T, Haskell T. Feedback interferometry with membrane mirror for adaptive optics. Optics Communication. 2003;**218**:33-41. DOI: 10.1016/S0030-4018(03)01188-X

[10] Shirai T, Barnes TH, Haskell TG. Adaptive wave-front correction by means of all-optical feedback interferometry. Optics Letters. 2000;**25**: 773-775. DOI: 10.1364/OL.25.000773

[11] Gu N, Huang L, Yang Z, Luo Q, Rao C. Modal wavefront reconstruction for radial shearing interferometer with lateral shear. Optics Letters. 2011; **36**:3693-3695. DOI: 10.1364/OL.36.003693

[12] Li D, Wang P, Li X, Yang H, Chen H. Algorithm for near-field reconstruction based on radial-shearing interferometry. Optics Letters. 2005;**30**: 492-494. DOI: 10.1364/OL.30.000492

[13] Liu D, Yang Y, Wang L, Zhuo Y. Real time diagnosis of transient pulse laser with high repetition by radial shearing interferometer. Applied Optics. 2007;**46**:8305-8314. DOI: 10.1364/AO.46.008305

[14] Hernandez-Gomez C, Collier JL, Hawkes SJ, Danson CN, Edwards CB, Pepler DA, et al. Wave-front control of a large-aperture laser system by use of a static phase corrector. Applied Optics. 2000;**39**:1954-1961. DOI: 10.1364/AO.39.001954

[15] Murty M, Compact Radial A. Shearing interferometer based on the law of refraction. Applied Optics. 1964; **3**:853-858. DOI: 10.1364/AO.3.000853

[16] Murty M, Shukla RP. Radial shearing interferometers using a laser source. Applied Optics. 1973;**12**: 2765-2767. DOI: 10.1364/AO.12.002765

[17] Ru Q-S, Ohyama N, Honda T, Tsujiuchi J. Constant radial shearing interferometry with circular gratings. Applied Optics. 1989;**28**:3350-3353. DOI: 10.1364/AO.28.003350

[18] Silva DE. Talbot interferometer for radial and lateral derivatives. Applied Optics. 1972;**11**:2613-2624. DOI: 10.1364/AO.11.002613

[19] Smartt RN. Zone plate interferometer. Applied Optics. 1974;**13**: 1093-1099. DOI: 10.1364/AO.13.001093

[20] Mohanty RK, Joenathan CJ, Sirohi RS. High sensitivity tilt measurement by speckle shear interferometry. Applied Optics. 1986;**25**:1661-1664. DOI: 10.1364/AO.25.001661

[21] Joenathan C, Torroba R. Simple electronic speckle-shearing-pattern interferometer. Optics Letters. 1990;**15**: 1159-1161. DOI: 10.1364/OL.15.001159

[22] Paterson C, Notaras J. Demonstration of closed-loop adaptive optics with a point-diffraction interferometer in strong scintillation with optical vortices. Optics Express. 2007;**15**:13745-13756. DOI: 10.1364/ OE.15.013745

[23] Bai F, Rao C. Experimental validation of closed-loop adaptive optics based on a self-referencing interferometer wavefront sensor and a liquid-crystal spatial light modulator. Optics Communication. 2010;**283**: 2782-2786. DOI: 10.1016/j. optcom.2010.03.032

[24] Bryngdahl O. Reversed-radial-shearing interferometry. Journal of the Optical Society of America. 1970;**60**: 915-917. DOI: 10.1364/JOSA.60.000915

[25] Mihaylova E, Whelan M, Toal V. Simple phase-shifting lateral shearing interferometer. Optics Letters. 2004;**29**: 1264-1266. DOI: 10.1364/OL.29.001264

[26] Kothiyal MP, Delisle C. Shearing interferometer for phase shifting interferometry with polarization phase shifter. Applied Optics. 1985;**24**: 4439-4447. DOI: 10.1364/ AO.24.004439

[27] Chung CY, Cho KC, Chang CC, Lin CH, Yen WC, Chen SJ. Adaptive-optics system with liquid-crystal phase-shift interferometer. Applied Optics. 2006; **45**:3409-3414. DOI: 10.1364/ AO.45.003409

[28] Naik DN, Ezawa T, Miyamoto Y, Takeda M. 3-D coherence holography using a modified Sagnac radial shearing interferometer with geometric phase shift. Optics Express. 2009;**17**: 10633-10641. DOI: 10.1364/ AO.17.010633

[29] Gu N, Yao B, Huang L, Rao C. A compact single-shot radial shearing interferometer with random phase-shift. Optics Letters. 2017;**42**:3622-3625. DOI: 10.1364/OL.42.003622

[30] Lago E, Fuente R. Amplitude and phase reconstruction by radial shearing interferometry. Applied Optics. 2007; **47**:372-376. DOI: 10.1364/AO.47.000372

[31] Li D, Wen F, Wang Q, Zhao Y, Li F, Bao B. Improved formula of wavefront reconstruction from a radial shearing interferograms. Optics Letters. 2008;**33**: 210-212. DOI: 10.1364/OL.33.000210

[32] Ragazzoni R, Marchetti E, Rigaut F. Modal tomography for adaptive optics. Astronomy and Astrophysics. 1999;**342**: L53-L56